國立中山大學化學系(所)

碩(博)士論文

Department/Institute of Chemistry

National Sun Yat-sen University

Master Thesis

奈米結構之石墨烯–鈷錳氧化物混成材料之合成及電化學催化應用

Synthesis of Nanostructured Graphene-Cobalt Manganese Oxide Hybrids for Electrochemical Catalysis Applications

研究生：藍文婕

Wen-Jie Lan

指導教授：陳軍互教授

Dr. Chun-Hu Chen

中華民國103年6月

June 2014

國立中山大學化學系

碩士論文

Department of Information Chemistry

National Sun Yat-sen University

Master Thesis

奈米結構之石墨烯-鈷錳金屬氧化物混成材料之合成及電化學催化應用

Synthesis of Nanostructured Graphene-Cobalt Manganese Oxide Hybrids for Electrochemical Catalysis

研究生：藍文婕

Wen-Jie Lan

指導教授：陳軍互 博士

Dr. Chun-Hu Chen

中華民國 103 年 6 月

June 2014

摘要

利用簡單之氧化還原方法將錳金屬參雜於鈷氧化物中並形成高表面積之三維奈米結構鈷錳金屬氧化物(CMO)，具有元素均勻分布及多重價態混價性質使其具有高導電度特性(1.5×10^{-2} S cm^{-1})，其導電度相較於一般鈷氧化物提升將近一千倍。利用溫度與時間作為變因，延長反應時間可使鈷錳氧化物之粒徑大小明顯增加，該金屬氧化物之表面結構因溫度上升明顯變多，且在反應溫度為 200 ^{o}C 時有雜相產生，故推測具兩個不同生長機制存在此氧化還原過程中。

石墨烯具高表面積與導電度之特性，常與金屬氧化物反應形成混成材料，且該混成材料可提升金屬氧化物之催化效能。在金屬氧化物經過表面修飾後，添加氧化石墨烯與金屬氧化物混成後再以水熱還原為石墨烯-鈷錳金屬氧化物(G-CMO#1, G-CMO#2, G-CMO#3)。此外針對不同石墨烯含量在過氧化氫還原的效能上有不同的效果，相較於 CMO 在過氧化氫偵測之靈敏度(0.23 μA mM^{-1})與線性範圍(0.5 mM -30 mM)，石墨烯混成樣品(G-CMO#3)大幅提升氧化氫偵測的靈敏度(11.01 μA mM^{-1})，但較小的線性範圍(5 μM -0.5 mM)。在本篇推測乃因石墨烯與 CMO 之奈米結構之間的關係以及石墨烯的含量所導致之差異。

關鍵字：多重混價、鈷錳金屬氧化物、石墨烯、混成、電催化

Abstract

A simple redox reaction was successfully conducted for the controlled synthesis of 3D flower-like cobalt manganese oxides (CMO) accompanying unique Y-shaped subunits with homogeneous elemental distribution and mixed-valence features, attributing to the highly conductive and reductive properties for electrochemical catalysis for sensing hydrogen peroxide and oxygen reduction reaction (ORR). The diameters and the nanoflakes of CMO spheres grew with the prolonged reaction time and raised temperatures. In addition, the nanowire impurity was obtained with reaction temperature at 200^{o}C for 24 hours. These results indicate that there two different growth paths dependent on the reaction temperatures.

Graphen with high conductivities and surface areas was used to generate the 3D flower-like graphene-cobalt manganese oxide composites (G-CMO) the optimal H_2O_2 and ORR performance. The surface treatment on CMO materials was first modified to possess counter charge to attract graphene oxide. Next, the as-obtained GO-CMO composites were treated hydrothermally to generate the reduced graphene oxide (G-CMO) composites. The sensitivity of G-CMO composites G-CMO#3 (11.01 μA mM^{-1}) is much higher than that of CMO. The linear range of G-CMO#3 (5 μM to 0.5 mM) is shorter than that of CMO (0.5 mM -30 mM). These results may due to the maturity of nanostructures on CMO and the graphene contents of G-CMO composites.

Keywords: mixed-valence, cobalt manganese oxide, graphene, hybridization, electrochemical catalysis.

Contents

List of Figures

List of Tables

1. Introduction

1-1. Controlled synthesis of controlled synthesis in binary metal oxides

Controlled synthesis is a concept of obtaining specific goals, such as unique morphology, specific crystal facets…*etc*, by changing conditions during the occurrence of reactions.[1] The normal controlled synthesis includes shape-control,[2-10] size-control,[11,12] crystal facet control,[13,14]…*etc*. Complicated systems in materials for specific applications can be demonstrated by controlled synthesis. To obtain a good morphology, uniform crystal phase, and specific elemental composition with a simple one-pot synthesis, however, is very difficult. Besides, to get better efficiency for wide applications such as electronics and fuel cells, homogeneous elemental distribution and mixed-valence feature in binary metal oxide materials are promising low-cost candidates, but difficult to manage. The co-precipitation[15-17] is widely used to produce binary metal oxides, but it is difficult to control the homogeneity in binary metal oxide system due to different precipitation rates (Ksp) among various metal ion precursors.

1-2. Redox method for binary metal oxides

Materials obtained by redox method may overcome the issue in homogeneous composition.[18] A redox reaction is highly restricted due to the appropriate redox potential and electron transfer numbers between the electron donating precursors and electron accepting precursors.[18] The intrinsically homogeneous composition of the materials will occur when they react with each other. The mixed-valence feature could be generated when redox reactions occur as well.

1-3. Applications of cobalt oxides

Due to the energy shortage and public health issues, high performance materials of photoelectronics and biosensors are desired. High conductivity and multiple valence states are necessary in materials generating the high performance for applications. For instance, the noble metals and their composites are those materials with high conductivity and multiple valence states. Nevertheless, the high cost and scarcity of noble metals limit their practical applications for sensors and electronics. On the other hand, the semiconductor transition metal oxides are good candidates to replace the noble metals in many applications due to excellent stability and low costs.

Cobalt oxide materials with spinel structure and mixed-valence structure are widely used in capacitors,[16,19,20] batteries,[21-23] fuel cells,[15,24-27] and biosensors.[28-31] Cobalt oxides are synthesized conventionally by precipitation,[32] microwave-assist reflux method,[20,33] chemical vapor deposition method,[34] solvothermal method,[22] and thermal decomposition.[35,36] The following statements to illustrate the methods of producing cobalt oxide:

Precipitation method[32] (Fig. 1) is defined that basic solutions, such as NaOH, KOH, NH_4OH, and urea solution, are added into cobalt (II) precursor solutions. The obtained precipitates are cobalt hydroxides ($Co(OH)_2$). After calcination of $Co(OH)_2$, cobalt oxides (Co_3O_4) are produced. Microwave-assist reflux method[20,33] (Fig. 2) is a concept of modified precipitate method. The basic solutions, such as NaOH, KOH, NH_4OH, and urea solution, are added into cobalt (II) precursor solutions. The mixture solutions are refluxed *via* microwave to produce $Co(OH)_2$. After calcination of $Co(OH)_2$, the cobalt oxides (Co_3O_4) are produced. Solvothermal method[22] is a route to make all precursor ions in the mixture solution react with each other under a high pressure atmosphere. After the interaction of cobalt ions under a high pressure

atmosphere, the Co_3O_4 was obtained. Thermal decomposition[35,36] is the Co (II) precursor powders, such as cobalt acetates, cobalt chlorides, are heated under high temperature in ambient atmosphere to generate cobalt oxide products. For good performance in these applications, high conductivities and surface areas are desired. However, these conventional methods mentioned are not easy to control the composition of dopant with good conductivities.

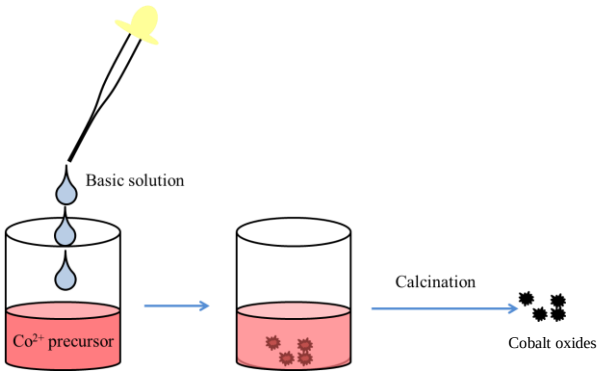

Fig. 2 Schematic illustration of precipitation method to form cobalt oxides

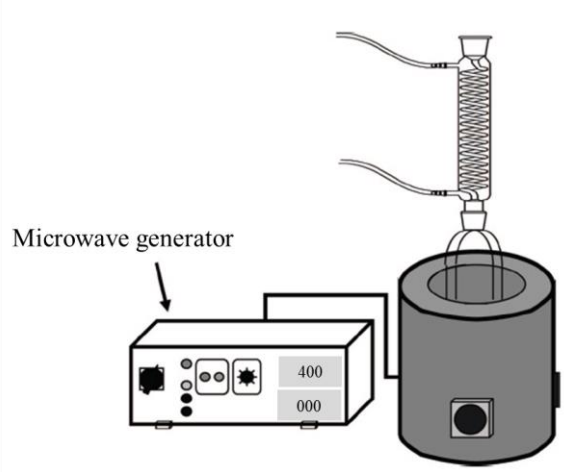

Fig. 1 The schematic of microwave-assisted reflux equipment.[20]

To obtain the high conductivity, manganese was doped into spinel cobalt oxide with redox procedure to get cobalt manganese oxides (CMO). The strong oxidant, potassium permanganate ($KMnO_4$) consumes the electrons of cobalt sulfate ($CoSO_4$), and forming cobalt manganese oxide hydroxide (CMOH) with homogeneous elemental distribution and mixed-valence feature. After calcination of CMOH, CMO was obtained with spinel structure of CMO. The eletrochemical activities of CMO for sensing H_2O_2 and oxygen reduction reaction are presented further. In addition, the time- and temperature-dependent reactions were performed to optimize the performance of CMO materials and discuss the growth mechanism of CMO.

1-4. Graphene hybridization

1-4-1. Purpose of using graphene

For improving the electrochemical activities of CMO for sensing hydrogen peroxide and oxygen reduction reaction, highly conductive graphene is a good candidate to hybridize with CMO. Due to excellent properties of graphene, including good charge mobility, high surface area and conductivities, and large mechanical strength,[37-39] hybridization of graphene with other material is an effective way to enhance the performance in many applications.[40,41]

1-4-2. Methods of preparing graphene

There are several ways to produce graphene. Micromechanical cleavage[42] (Fig. 3) is performed by sticky tapes and repeating exfoliation of graphite to form fewer layer graphene. Chemical vapor deposition method[43,44] (Fig. 4) is used to produce single layer graphene with CH_4 and H_2 on metal substrates at high temperature under

vacuum atmosphere. Liquid phase exfoliation[45-47] (Fig. 5) is done by ultrasonication of graphite with organic solvents, such as DMF, NMP, DMSO… *etc*. After sonication, the fewer layer graphene in the top of the suspension is obtained by centrifuge. Hummer's method[48-50] (Fig. 6) is a convenient, low-cast, and time-saving procedure to produce massive amount of graphene oxide. Then the graphene oxide can be further reduced to get reduced graphene oxide (rGO). These rGO can be used as the precursor for graphene composite materials. In our strategy, the Hummer's method was used to produce graphene oxide and hybridization with CMO due to the massive amount of graphene oxide and simple preparation procedure of graphene oxide.

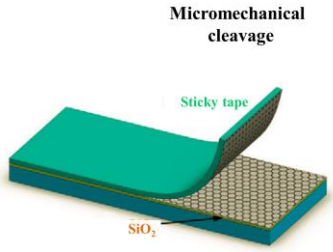

Fig. 3 Schematic illustration of micromechanical cleavage to form graphene.

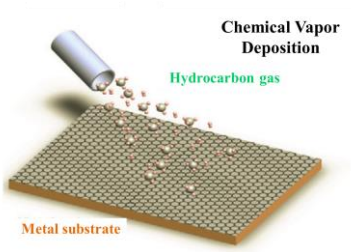

Fig. 4 Schematic illustration of CVD method to form graphene.

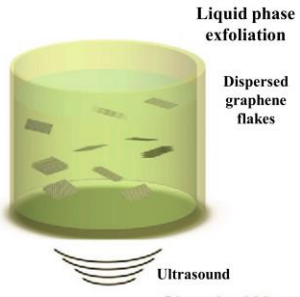

Fig. 5 Schematic illustration of liquid phase exfoliation to form graphene.

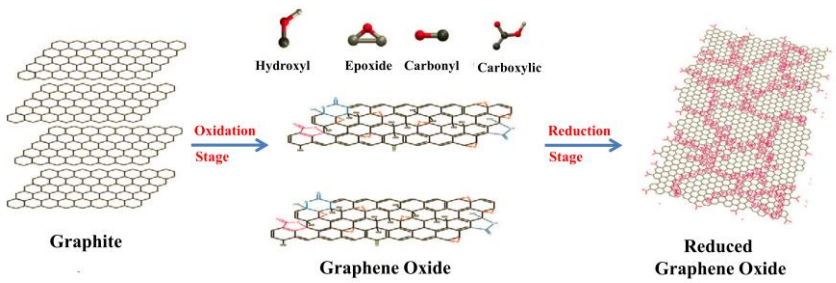

Fig. 6 Schematic illustration of the Hummer's method to form graphene.

1-4-3. How to synthesize the graphene-metal oxide composites

The normal method to synthesize of graphene-metal oxide composites is adding the graphene oxide solution into the precursor solutions of metal oxides.[51-55] Graphene nanosheets often are the substrates to support metal oxides. The graphene-based composites have high surface areas, but graphene contents are not easy to manage in this procedure.

1-5. Novelty and importance in this research

The homogeneous elemental composition and mixed-valence cobalt manganese oxides (CMO) was prepared by highly restrict redox method. Graphene-CMO composites were produced by two-step method. First, CMO was generated, next, graphene covered on the surface of CMO. This tow-step method can provide a prototype to improve the performance of the optimized metal oxide materials for electrochemical applications with controlling the contents of graphene without destroying the metal oxide materials.

2. Experimental Section

2-1. Reagents

Cobalt sulfate heptahydrate ($CoSO_4 \bullet 7H_2O$), potassium permanganate ($KMnO_4$), potassium chromate (K_2CrO_4) and Nafion solutions (5% in alcohols with 20% water) were provided from Sigma-Aldrich. Sulfric acid (98%) and hydrochloric acid (32%) was obtained from BASF Taiwan Ltd. Graphite powders (200 mesh) was supplied by Uni Region Bio-Tech. (3-aminopropyl)-diethyl-methylsilane (APTMS) was purchased from Alfa Aesar. Hydrogen peroxide solution (30%) was bought from Katayma Chemical Industry Company. Dopamine (DA), ascorbic acid (AA), urea acid (UA), glucose, and acetaminophenol were purchased from Acros Organucs. Potassium hydroxide (KOH) was supplied by Nihon Shiyaku Industry Company. Sodium dihydrogen phosphate (NaH_2PO_4) and disodium hydrogen phosphate (Na_2HPO_4) were bought from Panreac Co.

2-2. Synthesis

2-2-1. 3D Flower-like Cobalt - Manganese Oxide (CMO)

A purple solution was yield by mixing $CoSO_4 \cdot 7H_2O$ (8.08 mmol) and $KMnO_4$ (2.69 mmol) with 71 mL deionized water. The black precipitates were obtained after

cobalt precursor and manganese precursor mixed for 30 seconds. For hydrothermal treatment, the solution was transferred to a 125 mL Teflon-lined autoclave. The reaction was carried out at 100^{o}C for 24 hours and the resulting black precipitates were cleaned by washing with D.I. water for several times and then dried at 60˚C for 12 hours. The dried powder is cobalt manganese oxide hydroxides (CMOH) characterized by XRD. CMOH was calcined at 500^{o}C for 6 hours to generate cobalt manganese oxide (CMO) materials. For investigating the growth mechanism, the time- and temperature-dependent experiments were carried out. Time-dependent experiments were performed with different time intervals from 0.5, 1, 2, 4, 8, 12, and 24 hours at 100^{o}C. Temperature-dependent experiments were carried out with different temperatures at 60^{o}C, 80^{o}C, 100^{o}C, 150^{o}C, and 200^{o}C for 24 hours. The samples are defined as CMOH-60, CMOH-80, CMOH-100 (CMOH), CMOH-150, and CMOH-200. After calcination of CMOH materials, the obtained metal oxides are defined as CMO-60, CMO-80, CMO-100 (CMO), CMO-150, and CMO-200.

2-2-2. Cobalt – Chromium Oxide Hydroxide (CCOH)

Cobalt-chromium oxides were synthesized by reacting $CoSO_4 \cdot 7H_2O$ (8.08 mmol) and $KCrO_4$ (2.69 mmol) in 71 mL D.I. water to form a yellow solution, and the black precipitates were formed after cobalt precursor and manganese precursor mixed for 1

minute. The following steps of synthesizing CCOH were repeated from the preparation procedure of CMOH.

2-2-3. Graphene Oxide (GO)

Graphene oxide was synthesized from graphite based on the modified Hummers method.[48] Graphene oxide was prepared by mixing the flake graphite powder (1.0 g), sodium nitrate (0.5 g), and concentrated sulfuric acid (100 mL) for 30 min. Then potassium permanganate (6.0 g) was added into the mixture slowly under an ice bath. After the ice bath was removed, the reaction temperatures were brought to 50^{o}C for 16 hours. Deionized water (200 mL) and 23 mL of hydrogen peroxide were added into the suspension. Next, the suspension was filtered and washed with HCl (500 mL) and D.I. water to pH 6. The graphene oxide was exfoliated by ultrasonication (Branson S-450A with 400 W) for 30 min, followed by centrifugation with 14,000 rpm for 10 min to generate thin GO for hybridization with CMO.

2-2-4. G-CMO nanocomposites

First, CMO powder (0.4 g) was dispersed in 200 mL of ethanol by sonication (Elma E60H Elmasonic, 500 W) for 30 min. Afterward, suspension of CMO was mixed with 2 mL of (3-aminopropyl)- diethyl-methylsilane and refluxed at 80^{o}C for 12 hours. The precipitates were sufficiently rinsed with ethanol to wash away any

APTMS residue, and the resulting powder is APTMS-CMO. Different volume (50 mL, 100 mL, and 200 mL) of GO suspension with a concentration (0.2 mg mL^{-1}) was added into positively charged APTMS-CMO dispersion. After mixing for 30 min, the mixture was refluxed at 100^{o}C for 24 hours to yield GO-CMO. For the reduction of GO in GO-CMO, the GO-CMO nanocomposites were hydrothermally treated at 180^{o}C for 1 hour to produce rGO-CMO (G-CMO). G-CMO#1, G-CMO#2, and G-CMO#3 are defined as the different volume (50 mL, 100 mL, 200 mL) of GO suspension for hybridization with CMO. Besides, the CMO-60 was hybridized with GO to generate immature G-CMO#3.

2-3. Characterization

2-3-1. Scanning electron microscopy (SEM) studies

The dispersion of powder specimens in ethanol was dropped on a clean silicon wafer. The SEM studies were carried out by a Zeiss Supra 55 Gemini FE-SEM with a Schottky emitter operating at 1 kV and 5 kV with a beam current of 10 μA. The EDS experiments were done with X-MAX 20.

2-3-2. Transmission electron microscopy (TEM) studies

The powder specimens were dispersed in ethanol to form a suspension. The dispersion was dropped on the cupper grid (400 mesh) for TEM studies.

High-resolution TEM images were obtained in a Tecnai F20 Field Emission Gun Transmission Emission Microscope at 200 kV.

2-3-3. Crystalline analysis

Bruker D2 Phaser diffractometer with a CuKα X–ray source was used to obtain XRD patterns. Material powder was loaded on a sample holder, and the scan range 5– 85 degree (2θ).

2-3-4. BET studies

Nitrogen adsorption–desorption isotherms were measured with a Micromeritics ASAP 2010 instrument. The Brunauer–Emmett–Teller (BET) method was used to calculate the surface areas. The pore size distributions were derived from the Barrett–Joyner–Halenda (BJH) method.

2-3-5. TGA analysis

Contents of graphene in G-CMO composites were studied with thermogravimetry analysis (TGA). TGA was carried out using PerkinElmer TGA4000 thermal analyzer in O_2 with a flow rate of 20 mL/min at temperatures ranging from room temperature to 900℃ with a heating rate of 10 ℃ min^{-1}.

2-3-6. Conductivity:

The 0.15 g sample powder was compressed into a circular disk under a force of 400 kgw/cm^2. The conductivity measurements were performed with Quatek 5601Y Sheet Resistivity Meter 4 Point Probe.

2-3-7. Raman spectroscopy studies

The dispersion of powder specimens in ethanol was dropped on a clean silicon wafer. Raman spectra were recorded from 200 to 3000 cm^{-1} on a WITec Confocal Raman Microscope Alpha 300R using a 532 nm He-Ne laser.

2-3-8. X-ray photoelectron spectroscopy (XPS) studies

X-ray photoelectron spectroscopy (XPS) data were obtained using an Kratos Axis Ultra DLD X-ray photoelectron spectrometer equipped with an Al Ka X-ray source (1486.6 eV).

2-4. Electrochemical measurement:

2-4-1. Preparation of Material-modified Electrode

A smooth surface of glassy carbon electrode (GCE) plays an important role in good electrochemical activities. GCE of 3 mm in diameter was polished to a mirror-like surface *via* a 0.3 μm Al_2O_3 powder followed by rinsing with D.I. water, and repeating this step for 5 times to ensure that the surface of GCE is clean. For

electrochemical experiments, the electrodes were prepared by the following steps. First, 1 mg of catalyst powder and 1 mL of ethanol were mixed by sonication (Elma E60H Elmasonic, 500 W) for 30 min to form a homogeneous suspension. Then 10 μL of the homogeneous suspension was dropped on a GCE of 3 mm in diameter and dried at room temperature. Next, 10 μL of Nafion (0.1%) was loaded on top of the dried samples to get the modified electrodes for electrochemical measurements.

2-4-2. H_2O_2 Sensing Experiments

Cyclic voltammograms were recorded in potential ranged from -1.0 V to 1.0 V with a scan rate of 50 mV s^{-1} in a 1 mM H_2O_2. Chronamperograms were accomplished with a certain volume of H_2O_2 solution with various concentrations was injected into a 0.1 M phosphate buffer solution (PBS) at pH = 7.2, and the supplied potential is -0.5 V. The noise-level is obtained from the standard deviation of noise values; the sensitivities are defined as the slope values of the calibration curves. Electrochemical measurements were conducted using a three-electrode configuration using Ag/AgCl (saturate NaCl) as the reference electrode and Pt as the counter electrode, and the material modified electrodes as working electrodes in a CHI614D electrochemical analyzer.

2-4-3. Oxygen reduction reaction

The studies of oxygen reduction reaction were done by a three-electrode electrochemical cell using a reference electrode of Ag/AgCl (saturate NaCl), a Pt wire as a counter electrode, and the modified GCE working electrodes. The electrolyte (0.1 M KOH) was saturated with oxygen by bubbling O_2 for 20 min before starting each experiment. Oxygen was kept blowing into the electrolyte solution during the ORR experiment to ensure the O_2 content. The N_2-saturated KOH was obtained by bubbling N_2 for 20 min before starting each experiment.

3. Results

3-1. Synthesis and Growth Path of CMOH and CMO

3-1-1. Nanostructured Morphology and Crystal Structure

The nanostructured cobalt manganese oxide hydroxide (CMOH) materials were produced first by one-step hydrothermal reaction of cobalt and manganese at 100^{o}C for 24 hours, and then calcined at 500 ^{o}C for 6 hours to produce cobalt manganese oxide (CMO). The scanning electron microscopy (SEM) images of CMOH and CMO show the Y-shaped subunits constructing the three dimensional flower-like spheres (Fig. 7). The Y-shaped nanoflakes with thickness of 5-10 nm result in voids on CMOH and CMO sphere. The XRD patterns of CMOH and CMO are demonstrated in Fig. 8, indicating that the crystal phase are changed from CoOOH structure (JCPDS-07-169) to spinel Co_3O_4 (JCPDS-9-418) without any unexpected impurity phase.

High resolution TEM images (Fig. 9 a) are used to figure out the crystal structural correlation between the nanoflakes on CMO and macroscopic CMO powder. The solid CMO sphere was built with aggregation of nanoflakes. The lattice images in CMOH (Fig. 9 b) show a 4.40 Å spacing, corresponding to d_{003} in the CoOOH crystal

structure. In CMO (Fig. 9 d), the lattice fringes display a 2.85 Å spacing corresponding to d_{220} in the spinel Co_3O_4 structure.

3-1-2. Precursor Ratio Variation

To prove the multiple mixed-valence states in the materials forming by the redox method, the preparation experiments with different precursor ratios were performed. The results of EDXS and ICP-MS (Table. 1) show that the cobalt to manganese ratios in CMO changes very little despite the great ratios cobalt to manganese ratios in precursor solutions. Due to the restriction of redox reaction such as the electron numbers, Co/Mn ratios keep constant in CMO with different Co/Mn ratios in precursor solutions. In addition, the precipitates were not yielded when manganese was absent in precursor solutions during the reaction. The EDXS mapping experiments (Fig. 10) were used to acquire the elemental distribution in CMO. From the mapping results, cobalt and manganese distributed uniformly in the flower-like CMO sphere. The X-ray photoelectron spectroscopy (XPS) spectra (Fig. 11) are used to prove the multiple mixed-valence states in CMO material. The binding energy (BE) values of Co $2P_{1/2}$, Co $2P_{3/2}$, and the satellite peak of Co $2P_{3/2}$ in the CMOH are 781.1, 796.2, and 790.8 eV, respectively, corresponding to Co (III) .[56] After calcination, the BE of Co $2P_{1/2}$ and Co $2P_{3/2}$ are 779.8 and 795.0 eV respectively. The satellite peak at

790.8 eV vanishes in CMO. This phenomena shows a correlation with the mixed-valence of Co (II) and Co (III) in Co_3O_4.[57] The XPS spectra of Mn element in CMOH and CMO indicate that Mn $2P_{3/2}$ and Mn $2P_{1/2}$ with values of 642.5 and 654.2 eV, respectively, corresponding well on the Mn (IV).[58] It is difficult to define the mixed-valence states of manganese with XPS as the line-broadening effect.[57]

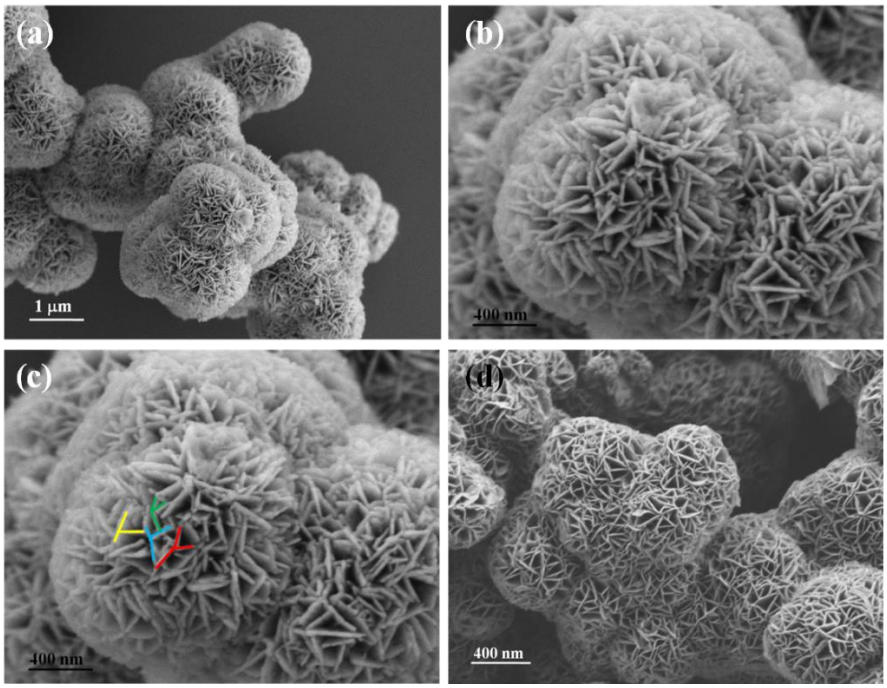

Fig. 7 The SEM images of cobalt manganese oxides. (a) CMOH; (b) the higher magnification images of CMOH; (c) the marks of Y-shaped subunits corresponding to the images in (b); (d) CMO obtained after the calcination of CMOH.

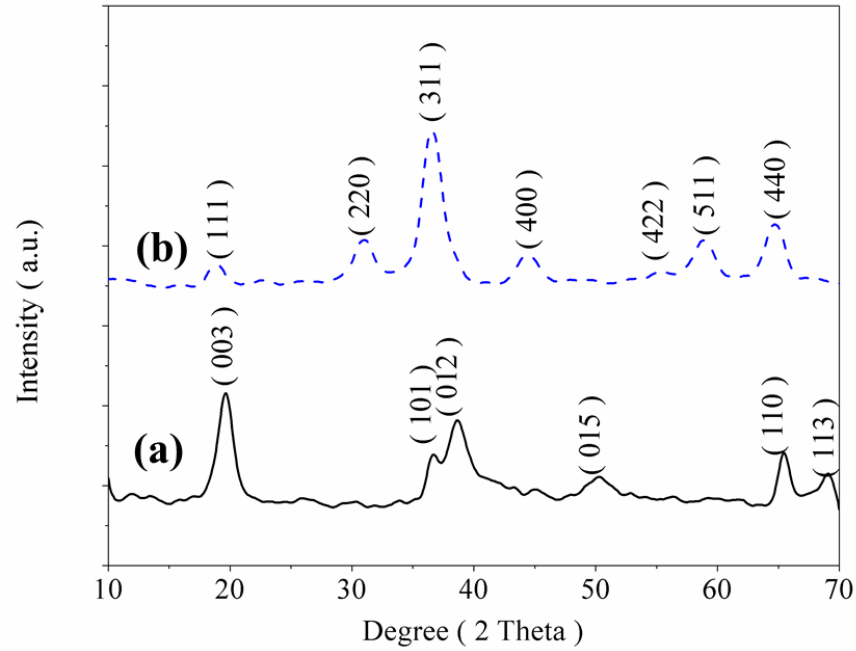

Fig. 8 The XRD patterns of the CMO products. (a) before calcination CMOH, and the calcined CMO (b).

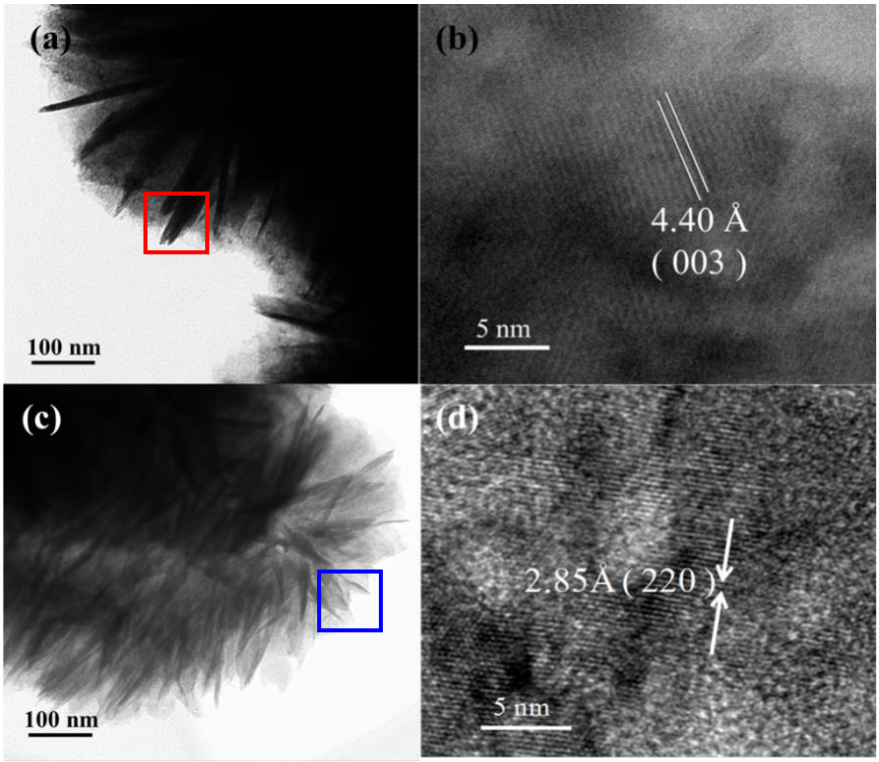

Fig. 9 The TEM images of CMO products. (a) uncalcined CMOH; (b) the HR-TEM images corresponding to the red square area in (a); (c) calcined CMO; the lattice fringes corresponding to the blue square area in (c).

Table 1 The elemental analyses of CMOH with different Co-to-Mn ratios.

Samples	ICP-MS (Co/Mn)	EDXS (Co/Mn)
CMOH (3:1)[a]	2.39	2.33
CMOH (4:1)[a]	2.66	2.62
CMOH (6:1)[a]	2.78	2.74
CMOH (10:1)[a]	2.99	2.95

[a] The Co-to-Mn ratios of precursors in the preparing process.

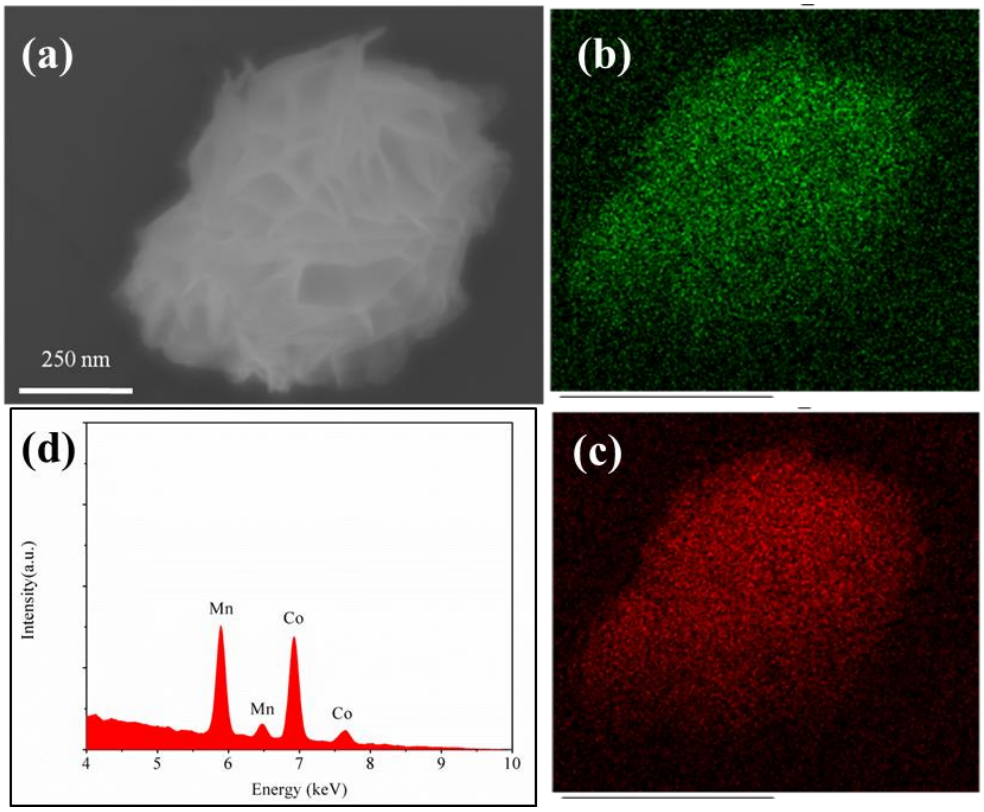

Fig. 10 The EDXS mapping of CMO. (a) SEM images of CMO sphere, (b) Co mapping of (a), (c) Mn mapping of (a), and (d) the elemental analysis of cobalt and manganese composition

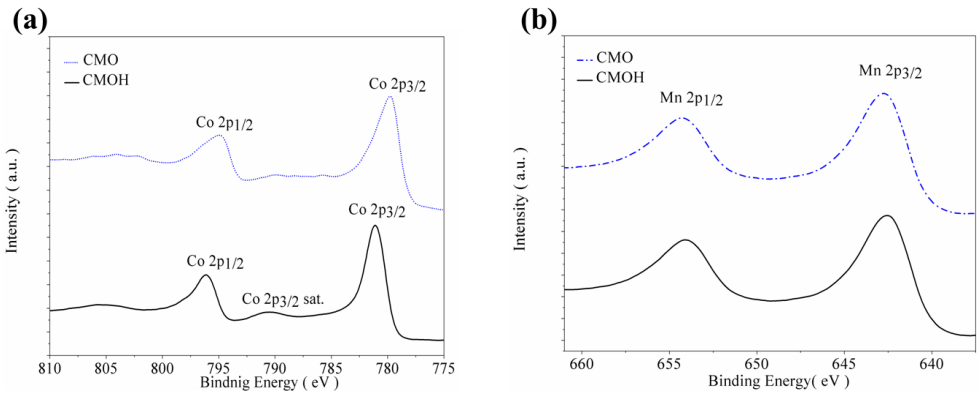

Fig. 11 T The XPS spectra of CMOH and CMO. (a) Co 2P and (b) Mn 2P.

3-1-3. Time-dependent and Temperature-dependent Experiments

To find out the growth path of the flower-like in CMOH, time- and temperature-dependent experiments were conducted. In time series experiments (Fig. 12), the sphere with diameters of 100-200 nm, but no Y-shaped subunit or flower-like nanostructure were obtained after reacting for 0.5 hours (Fig. 12 a). After 1 hour (Fig. 12 b), the nanostructures were generated on the surface of CMOH because the nanoflakes started growing, and the particle diameter enlarged to 300 nm briefly. After 4 and 8 hours, the Y-shaped nanoflakes are observable on the CMOH sphere. After 24 hours, the diameter of CMOH sphere grew to 1 μm (Fig. 12). In addition, the XRD patterns (Fig. 13) of CMOH with different reaction time (0.5, 1, 2, 4, 8, 12, and 24 hours) are investigated to confirm that the crystal structure of the CMOH sphere. Furthermore, no impurity was observed in SEM and XRD with the prolonged time.

Temperature-dependent experiments (Fig. 14) were conducted at 60^{o}C, 80^{o}C, 120^{o}C, 150^{o}C, and 200^{o}C for 24 hours. The samples were defined as CMOH-60, CMOH-80, CMOH-120, CMOH-150, and CMOH-200. The SEM images of CMOH-60 (Fig. 14 a) demonstrate that the diameters of sphere are 400-500 nm, and the Y-shaped subunits were formed but not observable on the surface. The SEM

images of CMOH-80 (Fig. 14 b) show that the voids were constructed by nanoflakes and forming spheres with the diameter were 0.8-1 μm. The void space increased with the elevated temperature. The SEM images of CMOH-150 (Fig. 14 e) indicated that the nanoflakes and voids on CMO sphere become bigger than CMOH-60 and CMOH-80 with diameter of sphere was 3μm. The images of CMOH-200 demonstrated that the nest-like features were obtained comprised of nanowire impurity covering on the surface of the 3-D flower-like spheres. In addition, the γ-MnO_2 phase characterized by XRD (Fig. 15 d) was generated in CMOH-200. The growth process of CMOH-200 is based on SEM results (Fig. 15). The bulk star-like materials (Fig. 15 a) was obtained in CMOH-200, and the 3D flower-like spheres were located on the center and edges of the star-like materials (Fig. 15 b). The SEM images of the edge of star-like materials at higher magnification indicate that the nanowires (red arrows) exfoliated from the edges (green arrows) of the star-like materials. Furthermore, the nanowires covered on CMO spheres and forming a nest-like CMOH-200 (Fig. 15 c). The elemental composition of CMOH-200 was studied with EDXS (Fig. 16). The results indicate that manganese content is much higher than cobalt in star-like materials but the same as cobalt in 3D flower-like sphere. Cobalt was introduced in the star-like materials during the redox procedure,

and the manganese was introduced in the 3D flower-like sphere. The impurity nanowires were generated at 200^{o}C, and there is a competition between two pathways during the hydrothermal process.

$$3\ Co^{2+} + Mn^{7+} \rightarrow 3\ Co^{3+} + Mn^{4+} \quad (1)$$

$$4\ MnO_4^- + 2\ H_2O \rightarrow 4\ MnO_2 + 4\ OH^- + 3\ O_2 \quad (2)$$

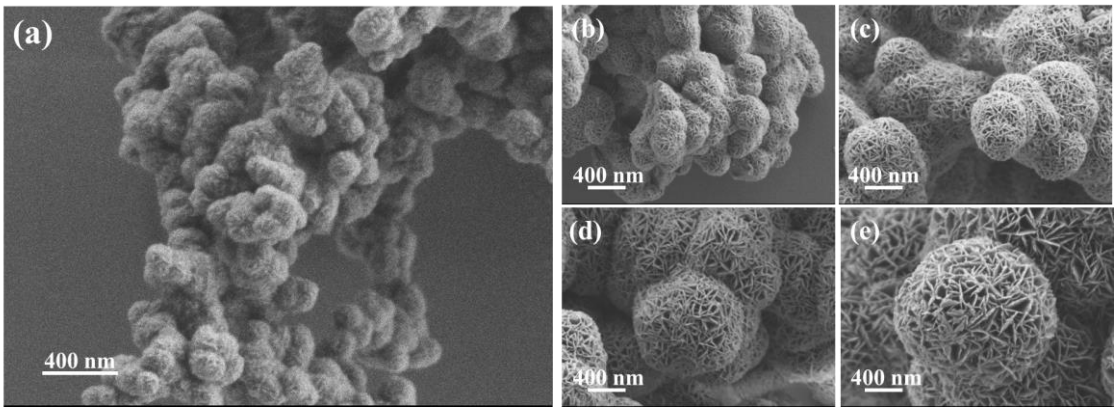

Fig. 12 The SEM images of CMOH with different reaction time. (a) 0.5 hours, (b) 1 hour, (c) 2 hours, (d) 4 hours, (e) 8 hours.

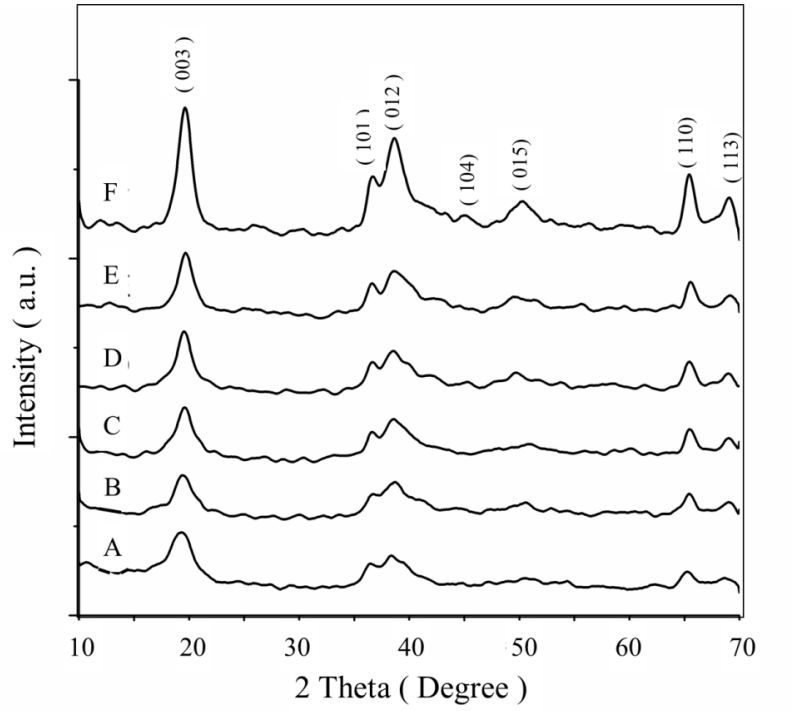

Fig. 13 The XRD patterns of CMOH with different reaction time. (A) 0.5 hours, (B) 1 hour, (C) 2 hour, (D) 4 hours, (E) 12 hours, (F) 24 hours.

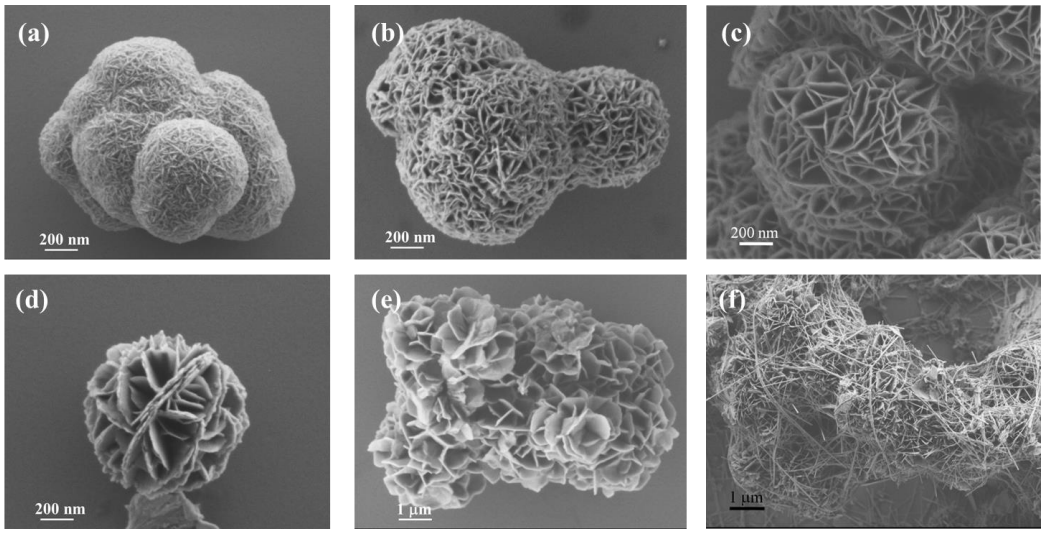

Fig. 14 The SEM images of CMOH at different reaction temperatures. (a) CMOH-60 (b) CMOH-80, (c) CMOH-100, (d) CMOH-120, (e) CMOH-150, and (f) CMOH-200.

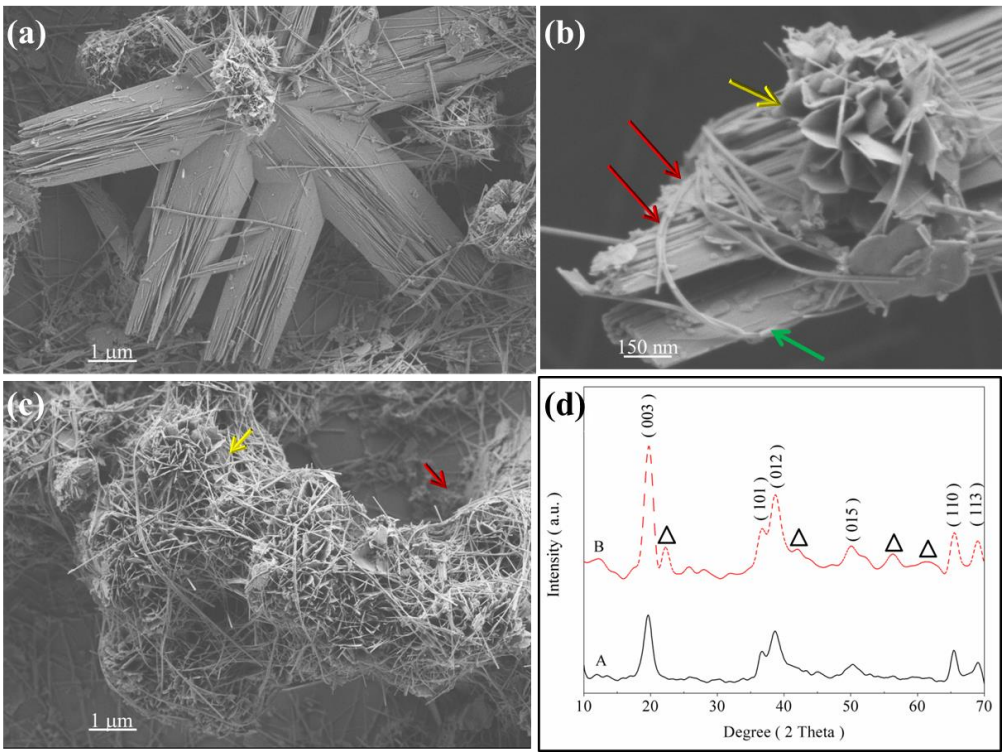

Fig. 15 The SEM of CMOH-200. (a) 3D flower-like sphere on star-like bulk materials, (b) the nanowires (red arrows) and the edges (green arrows) of star-like materials, (c) the nest-like CMOH-200 with nanowires (red arrow) and 3D flower-like sphere (yellow arrow), (d) The XRD patterns of (A) CMOH-100, (B) CMOH-200 with the γ-MnO_2 phase labeled triangle mark with CoOOH crystal structure.

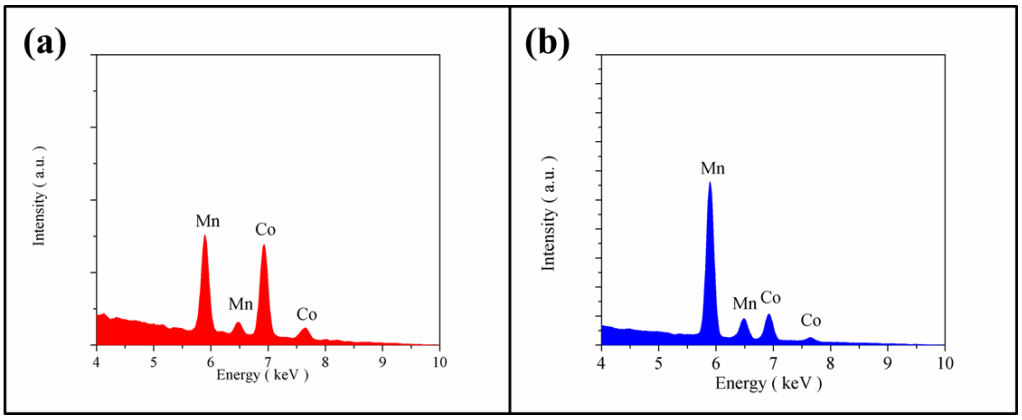

Fig. 16 The elemental analysis of CMOH-200. (a) 3D flower-like spheres and (b) star-like bulk materials.

3-2. Synthesis of CCOH with redox method

The cobalt chromium oxide hydroxide (CCOH) was produced to prove that the redox method could be a general procedure for yielding binary metal oxides. The SEM images of CCOH (Fig. 17 a and Fig. 17 c) are demonstrated that the thickness (10-20 nm) of CCOH nanoflakes is thicker than CMOH and the voids are not detectable. The elemental analysis (Fig. 17 b) is shown that the chromium and cobalt were present in CCOH. The crystal structure of CCOH corresponds to single phase of CoOOH (JCPDS-07-169) by analyzing XRD patterns (Fig. 17 d). These results indicate that Cr^{6+} consumes the electron from Co^{2+} and forming a single phase binary metal oxide, such as CMO.

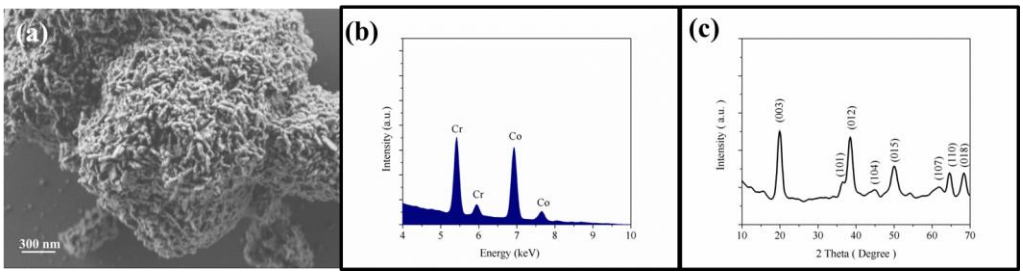

Fig. 17 The characterization results of CCOH. (a) SEM images of COOH, (b) the elemental analysis of CCOH, and (c) the XRD patterns of CCOH.

3-3. Graphene Hybridization and Effects of Graphene Oxide

3-3-1. Synthesis and Characterization

Graphene-cobalt manganese oxide was obtained *via* the electric attraction between graphene and CMO modified by (3-aminopropyl)-diethyl-methylsilane (APTMS). Morphology of G-CMO materials was studied by SEM (Fig. 18). CMO without graphene was demonstrated in Fig. 18 a. The graphene sheets (red arrows) cover on the surface of CMO. SEM images indicate that the area of graphene sheets covering on the CMO surface is increased with the raised volume of GO suspension added for hybridizing with CMO. Second, the Y-shaped subunits (green marks) of CMO are still observable with graphene coverage in G-CMO#3. The interfaces of G-CMO materials for electrochemical applications are changed by the amplified addition of GO suspension.

TEM images (Fig. 19) show the interfaces between graphene and CMO. The TEM images of G-CMO#1 (Fig. 19 a) indicate that the coverage of graphene on CMO is less than the ones in G-CMO#3 (Fig. 19 c). The HR-TEM images of G-CMO#3 (Fig. 19 d) demonstrate that graphene is increased and filled in the inter-flake space in G-CMO#3. Different interfaces of graphene and CMO in G-CMO can be controlled by raised volume of GO suspension for hybridization with CMO and cause the

distinct performance of G-CMO for sensing H_2O_2. The lattice images of G-CMO#1 (Fig. 19 b) show a 4.40 Å spacing, corresponding to the d_{111} in the spinel Co_3O_4 (JCPDS-9-418) crystal structure. Lattice fringes of G-CMO#3 (Fig. 19 d) display that a 2.43 Å spacing which corresponds to the d_{311} in the spinel Co_3O_4 structure. After hydrothermal treatment for reduction of GO-CMO, the crystal structure and morphology were not changed, and the CMO can be hybridized with graphene without damage.

XRD patterns (Fig. 22a) show that the crystal structure of CMO is very stable because the crystal phase remains the same after modification of CMO and reduction of GO-CMO. Selected Area Electron Diffraction (SAED) patterns further confirms the Co_3O_4 phase identified by XRD results.

Raman spectrometer is a sensitive instrument to detect carbon materials. The Raman spectra (Fig. 23a) can identify the presence of graphene G-CMO materials. D-band and G-band peak in rGO and G-CMO materials corresponds to 1356 cm^{-1} and 1600 cm^{-1}, respectively.[51,59] X-ray photoelectron spectroscopy (XPS) is used to judge whether GO is reduced after hydrothermal treatment. XPS spectra (Fig. 23 b) of GO-CMO and G-CMO, four peaks center at 284.5, 286.7, 287.8, and 288.8 eV that refer to the bonding type of sp^2 C, C-O, C=O, and O-C=O, respectively.[51,60]

Moreover, the intensities of C-O and O-C=O are decreased after the GO-CMO was reduced hydrothermally.

Contents of graphene covering on CMO were measured by thermogravimetric analysis (TGA). Results of TGA (Fig. 24) are demonstrated that graphene decomposed at 300^{o}C. CMO show a good thermal stability from room temperature to 600^{o}C. Moreover, weight loss and graphene contents of each material are summarized in Table. 2, indicating that the graphene contents of G-CMO materials are proportional to the mass of GO used to hybridize with CMO.

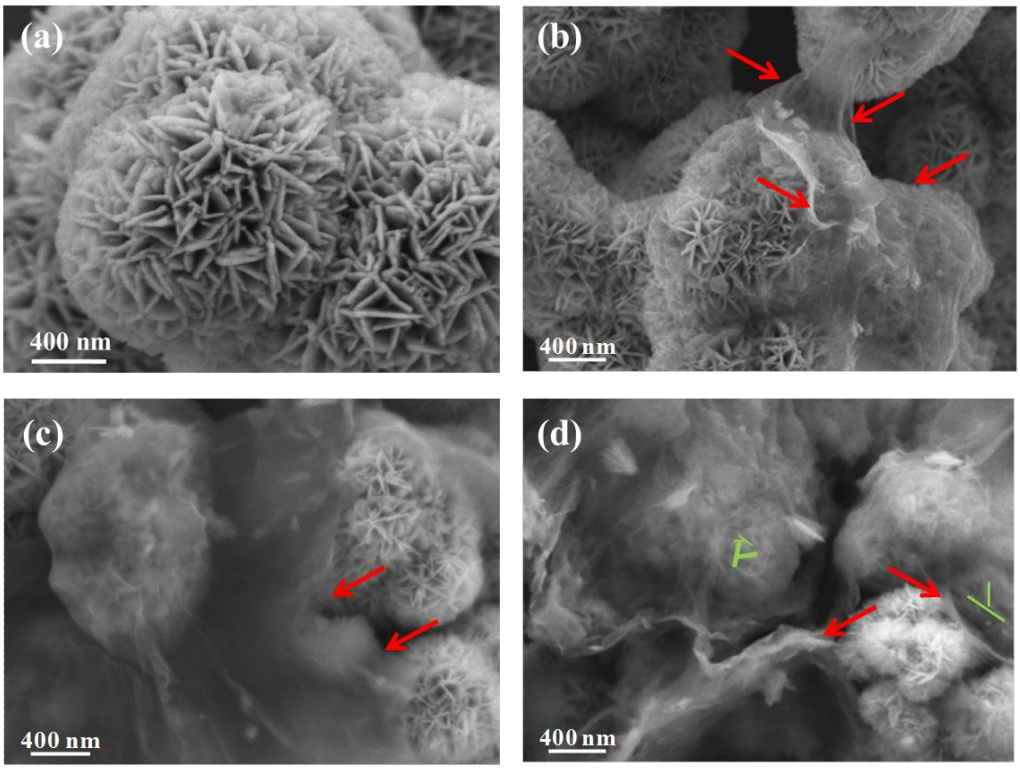

Fig. 18 The SEM images of different graphene content of G-CMO materials. (a) CMO, (b) G-CMO#1, (c) G-CMO#2, and (d) G-CMO#3. Red arrows display graphene and green Y-marks represent of the Y-shaped subunits of CMO.

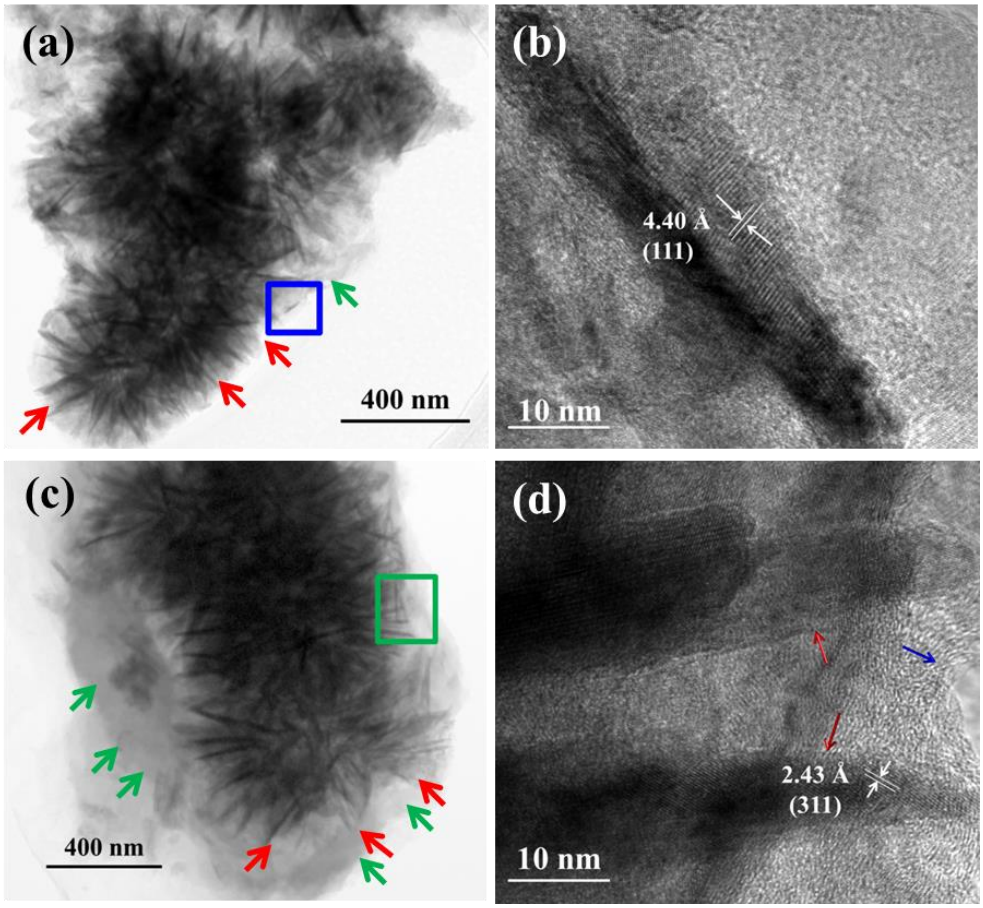

Fig. 19 The TEM images of G-CMO materials. (a) G-CMO#1 and (c) G-CMO#3; the lattice images of G-CMO materials. (b) G-CMO#1 corresponding to the blue square area in (a), and (d) G-CMO#3 corresponding to green square area in (d). Red arrows represent nanoflakes of CMO and green arrows indicate of graphene.

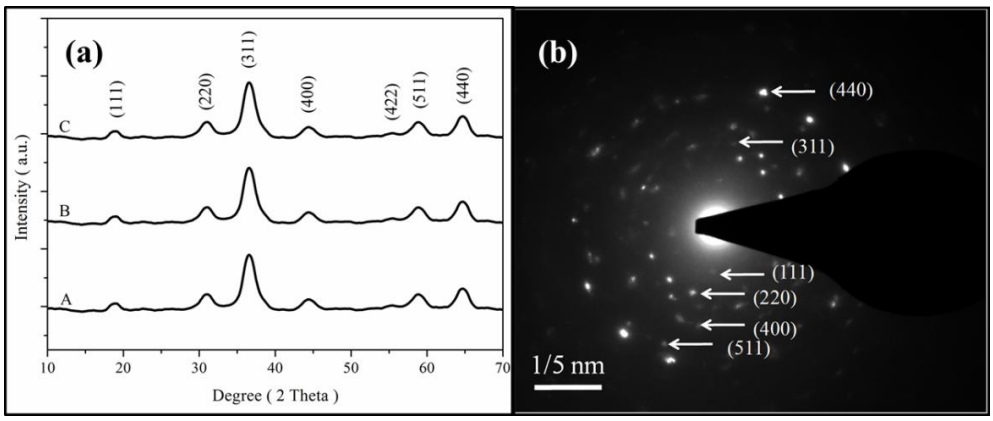

Fig. 20 The XRD patterns of different products. (A) CMO, APTMS-CMO (B) and (C) G-CMO; (b) the SAED patterns of G-CMO corresponding to blue square area in Fig 14(a).

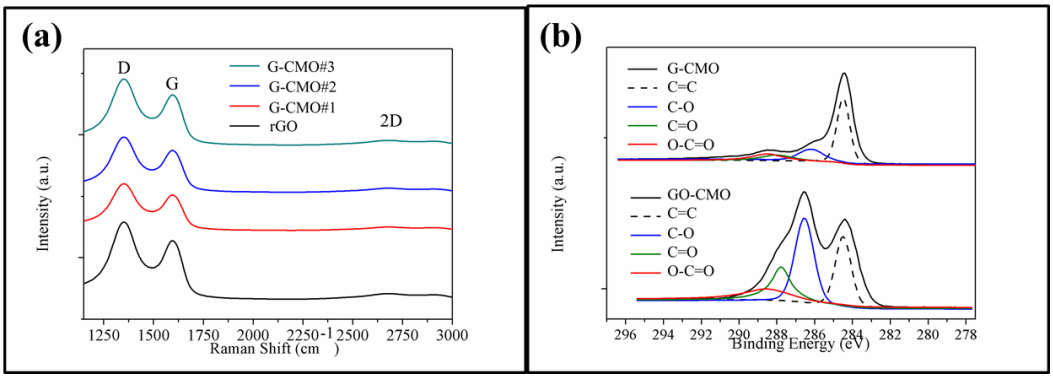

Fig. 22 The Raman spectra of GO, G-CMO#1, G-CMO#2, and G-CMO#3; (b) the XPS spectra of GO-CMO and G-CMO.

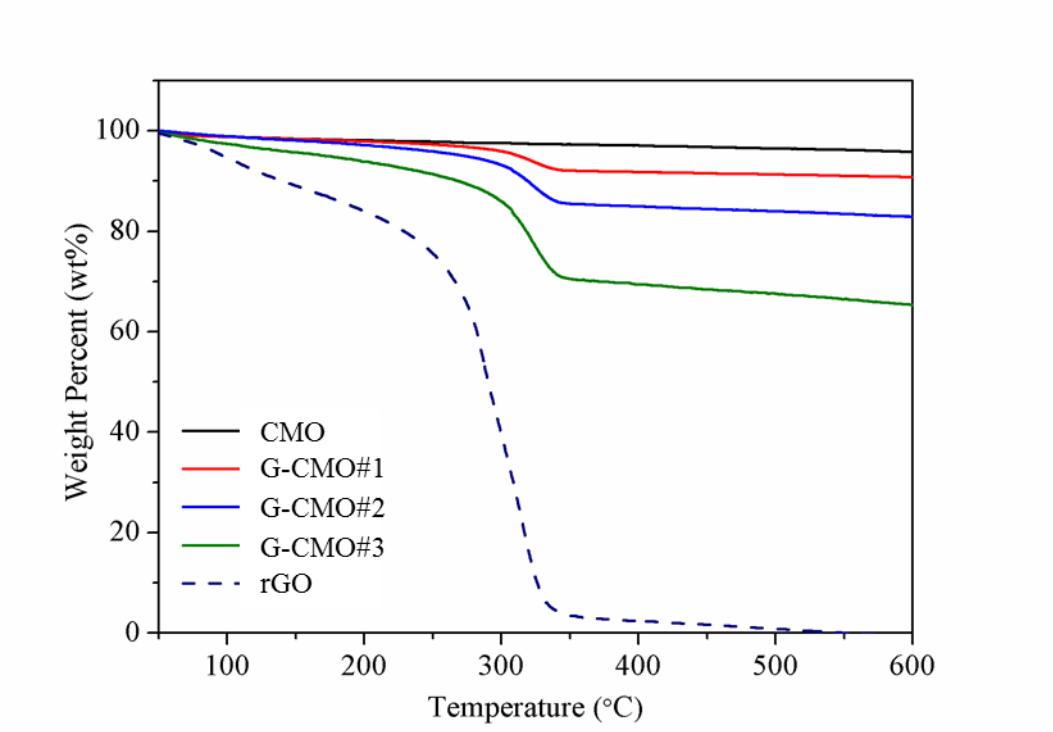

Fig. 21 TGA of CMO (black line), G-CMO#1 (red line), G-CMO#2 (blue line), G-CMO#3 (green line), and rGO (blue-dash line).

Table 2 The summary of weight loss of rGO covered on surface of CMO.

Sample	**CMO**	**G-CMO#1**	**G-CMO#2**	**G-CMO#3**
Weight Loss (wt %)	0.3	3.6	7.13	15.8
Graphene content ratio*	0	1	2	4

* The graphene content ratio was defined by the weight loss.

3-3-2. Physical properties of CMO and G-CMO materials

Physical properties and chemical composition of temperature-dependent CMO materials are included in Table. 3. Conductivity values and surface areas increase with declined of Co/Mn ratios in CMO materials. As temperature raise, the resulting Co/Mn ratios become lower; the two different grow pathways are inferred in discussion part later. The conductivities are highly enhanced after doping Mn into Co_3O_4. The conductivity values of CMO are 3 orders higher than Co_3O_4. In addition, conductivities and surface areas of CMO and G-CMO are summarized in Table. 4. Conductivity values and surface areas of G-CMO materials were enhanced after the CMO hybridization with graphene.

Table 3 The summary of surface areas, conductivities, and chemical compositions of CMO samples.

Sample	**CMO-60**	**CMO-100**	**CMO-150**	**Co_3O_4 ***
Conductivity ($S\ cm^{-1}$)	0.9×10^{-2}	1.5×10^{-2}	2.9×10^{-2}	3.1×10^{-5}
Surface area ($m^2\ g^{-1}$)	42	57	58	–
Co/Mn ratio[a]	3.0	2.6	2.3	–

CMO-60 and CMO-150 were obtained after calcination of CMOH-60 and CMOH-150.

* The conductivity value of Co_3O_4 is from ref.15. [a] The data were obtained from EDXS equipment.

Table 4 The summary of conductivity and surface areas of G-CMO samples.

Sample	**CMO**	**G-CMO#1**	**G-CMO#2**	**G-CMO#3**
Conductivity ($S\ cm^{-1}$)	1.5×10^{-2}	2.1×10^{-1}	4.5×10^{-1}	7.3×10^{-1}
Surface area ($m^2\ g^{-1}$)	57	83	104	200

3-4. Electrochemical activities of CMO and G-CMO materials

3-4-1. Candidate of G-CMO Materials

For testing electrochemical activities of the materials, the sensing of hydrogen peroxide and the oxygen reduction reaction were performed. The CVs results demonstrate that the current value of CMO is 2.2 times larger than commercial Co_3O_4 and 6.2 times than GCE respectively (Fig. 23 a). To choose the best CMO-candidate for hybridization with graphene, the comparison of CMO-60, CMO, and CMO-150 was conducted in the presence of H_2O_2. Obviously, the current value of CMO is higher than that of CMO-150 by 112% and CMO-60 by 180% (Fig. 23 b). These results are due to the morphology of CMO spheres prepared at different temperatures.

3-4-2. Electrochemical activities of CMO and G-CMO materials for sensing H_2O_2

As CMO was hybridized with different amounts of graphene, the electrochemical H_2O_2 sensing activities of the CMO and G-CMO composites (Fig. 24) were measured. CVs in H_2O_2 (1 mM) (Fig. 24 a) display that the current values of G-CMO#1, G-CMO#2, and G-CMO#3 are 1.7, 2.4, and 2.4 times larger than CMO, respectively. In particular, onset potential value of G-CMO#3 is 0.6 times lower than that of CMO.

The amperometric response of G-CMO#1 (Fig. 26 c) and G-CMO#3 (Fig. 26 d) in a PBS under continuous changes of H_2O_2 concentration is demonstrated that the linear range of G-CMO#3 (5 μM to 0.5 mM) is shorter than the one of G-CMO#1 (0.5 mM to 34 mM). The sensitivities of commercial cobalt oxide, CMO, G-CMO#1, and G-CMO#3 are 0.0038, 0.23, 0.71, and 11.01 μA mM^{-1}, respectively. The calculated detection limits of G-CMO#1 and G-CMO#3 are 250 μM and 150 μM with single-to-noise ratio of 3. The actual detection limits of G-CMO#1 and G-CMO#3 were 50 μM and 5 μM, respectively.

The selectivity of G-CMO#1 (Fig. 25 a) and G-CMO#3 (Fig. 25 b) were investigated in the presence of interference species, such as dopamine (DA), urea acid (UA), ascorbic acid (AA), glucose, and actaminophenol. Both G-CMO#1 and G-CMO#3 are highly selective in the presence of H_2O_2 (0.1 mM) at -0.5 V supplied potential. These results display excellent anti-interference properties similiar to noble metal biosensors.

3-4-3. Synergistic effect of G-CMO

The CVs of rGO synergistic effects (Fig. 26)of hybridization of rGO and CMO were demonstrated. Both rGO and CMO have reductive peaks in the presence of H_2O_2 with 0.1 M PBS (Fig. 26 a). The current value of G-CMO#3 is not only much

larger than the ones of rGO and CMO, but the onset potential of G-CMO#3 is also much lower than the one of rGO by 0.1 V and CMO by 0.2 V. Moreover, the ORR activities of G-CMO samples were demonstrated with CVs in the presence of O_2 with 0.1 M of KOH. The onset potential of rGO is slightly higher than G-CMO#3, while that of CMO is higher than G-CMO#3 by 0.13 V. The results indicate that the synergistic effect was established by the hybridization of rGO and CMO.

3-4-4. Nanostructure effect of CMO for hybridization

The CMO-60 was hybridized with rGO to form immature G-CMO#3 to understand the effect of nanostructure in rGO and CMO hybridization. The onset potential of G-CMO#3 is lower than immature G-CMO#3 by 0.05 V (Fig. 27). The current value of G-CMO#3 is 2 times higher than immature G-CMO#3. The interfaces between CMO and rGO were studied with TEM images. The nanoflakes of immature G-CMO#3 (Fig. 28 a) are shorter than these of G-CMO#3 (Fig. 28 b). These results lead to the hybridization between CMO-60 and rGO is less effective than that between CMO and rGO, which might due to larger void spaces to be filled with greater amount of graphene.

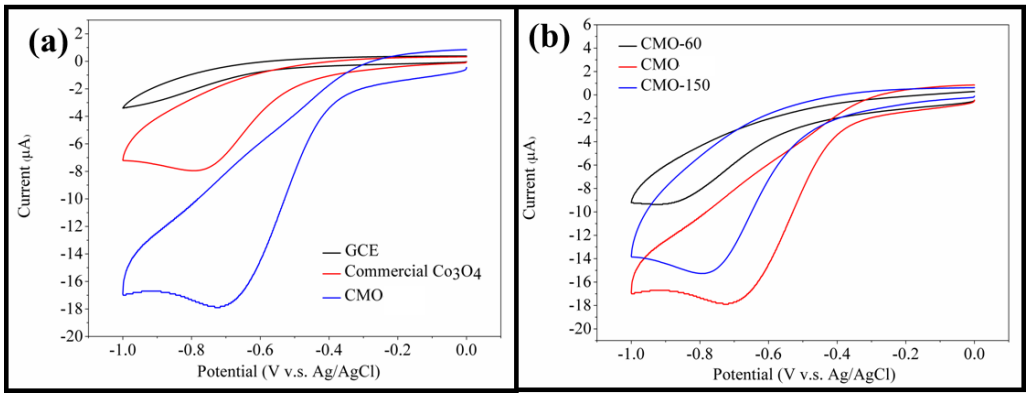

Fig. 23 Cyclic voltammograms (CVs) of different electrodes in a 1mM of H_2O_2 with a 0. 1 M PBS. (a) blank GCE (black line), commercial Co_3O_4 (red line), and CMO (blue line), (b) CMO-60 (black line), CMO (red line), CMO-150 (blue line).

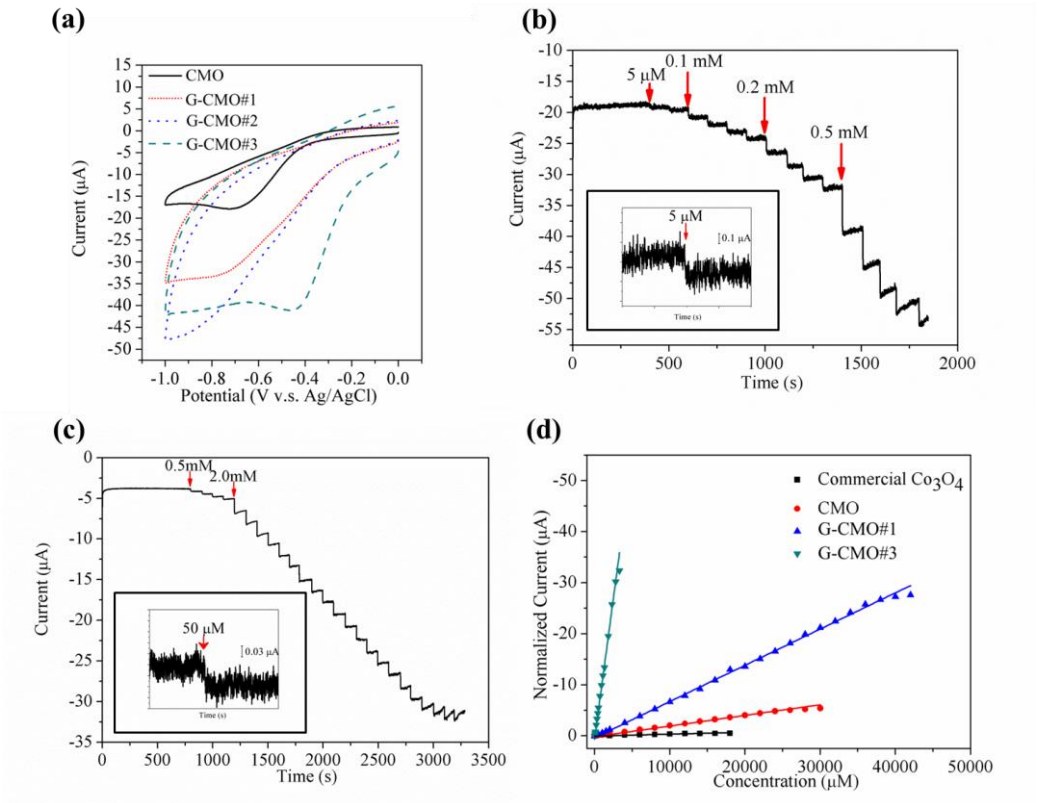

Fig. 24 The electrochemical studies of G-CMO materials for H_2O_2 sensing. (s) CVs of various electrodes in a 1mM of H_2O_2 with 0.1 M PBS. (a) CMO (black line), G-CMO#1 (red-dot line), and G-CMO#2 (blue-short dash line), and G-CMO#3 (green-dash line); (b) the amperometric response of G-CMO#3 at -0.5 V with continuous additions of H_2O_2, the inset is the detection limit of G-CMO#3, (c) the amperometric response of G-CMO#1 at 0.5 V with continuous addition of H_2O_2, (d) the calibration curves of commercial Co_3O_4 (black line), CMO (red line), G-CMO#1 (blue line), and G-CMO#3 (green line).

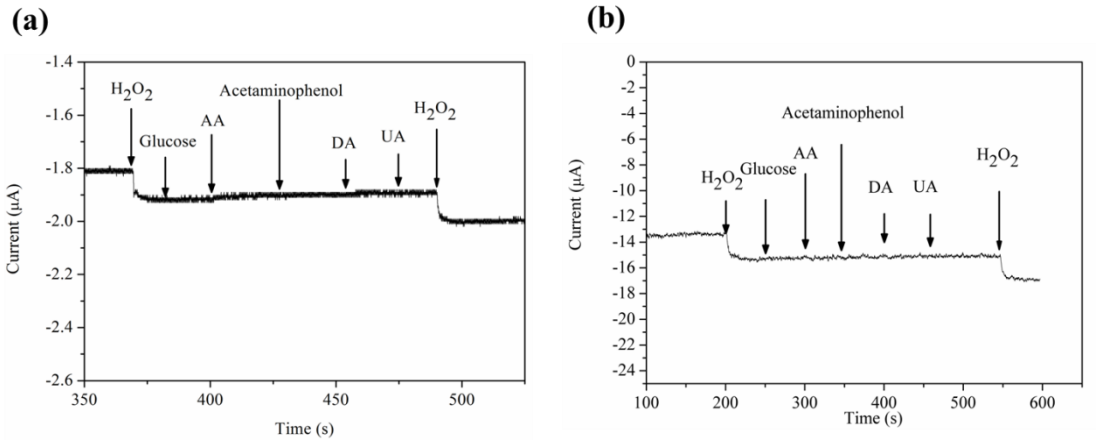

Fig. 25 The current-time curves for interference studies of H_2O_2 sensing with the presence of interfering species of 0.1 mM DA, UA, AA, and acetaminophen as well as glucose (5 mM). (a) G-CMO#1 and (b) G-CMO#3

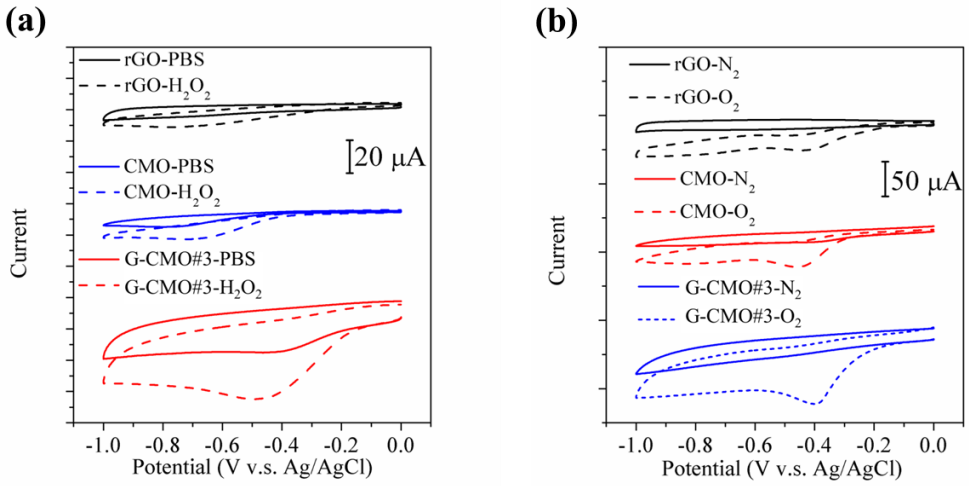

Fig. 26 CVs of rGO, CMO, and G-CMO#3 in a 1mM of H_2O_2 or PBS (a), CVs of rGO, CMO, and G-CMO#3 for oxygen reduction reaction (ORR) in O_2-saturated (dash line) or N_2-saturated (solid line) 0.1 M KOH.

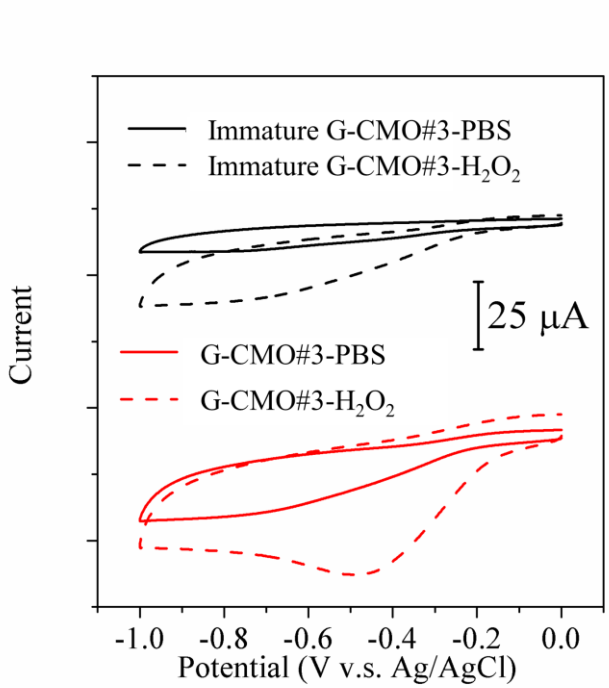

Fig. 27 CVs of immature G-CMO#3 and G-CMO#3 in a 1mM of H_2O_2 (dash line) or a 0.1 M of PBS (solid line)

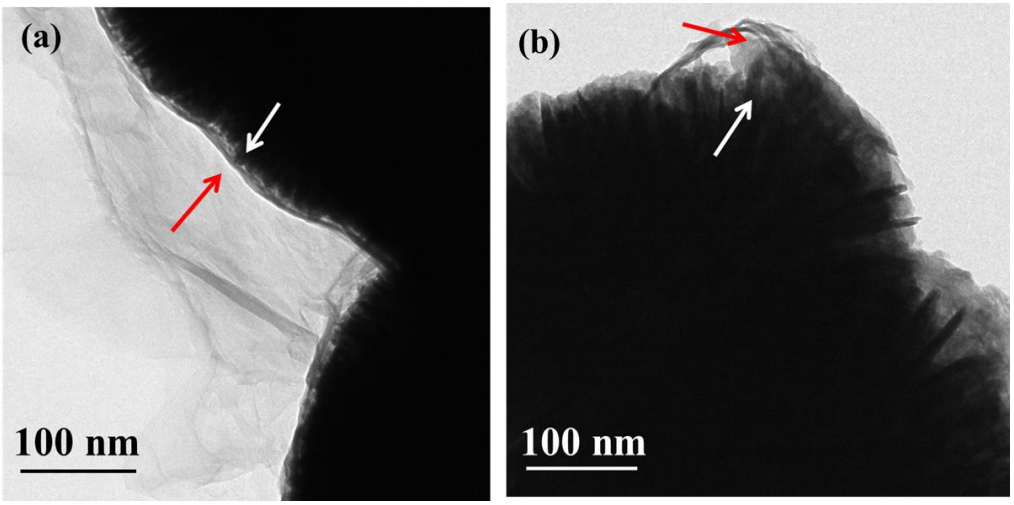

Fig. 28 TEM images of G-CMO samples. (a) immature G-CMO#3 (b) and G-CMO#3. Nanoflakes (white arrow) and rGO (red arrow)

4. Discussion

4-1. Growth path and mechanism of CMO

Growth path of CMOH was studied by time- and temperature-dependent experiments. First of all, the reaction time with 0.5 and 1 hour are defined as nucleation period. The Y-shaped subunits and nanostructures were not obtained for CMOH with reaction time of 0.5 hours and 1 hour with the spherical diameters of 50-100 nm. The intensities in XRD patterns are weak compared to other CMO samples. Secondly, the reaction time with 2, 4, and 8 hours are defined as growing period. The growth of Y-shaped subunits as well as spherical diameter is pronounced. The final stage, mature period, is defined by the reaction time of 24 hours. The Y-shaped subunits are mature, and the surface voids between nanoflakes on CMO are fairly large.

The temperature-dependent results show that the Y-shaped subunits become more observable with raising temperature, and the manganese contents increase as well. Particularly, two distinguishable morphologies with nanowires and 3D flower-like spheres form a nest-like morphology in CMOH-200. Besides, elemental compositions of materials produced by temperature-dependent experiments indicate that there are two different potential growth paths competing each other under the

hydrothermal condition. XPS spectra of CMOH show that both Co^{3+} and Mn^{4+} are the major species. So the main growth process in lower reaction temperatures (60°C, 80, 100, and 150°C) is following euation below:

$$3\ Co^{2+} + Mn^{7+} \rightarrow 3\ Co^{3+} + Mn^{4+} \qquad (1)$$

The elemental composition of CMOH-200 shows two different situations. Manganese contents in nanowires are higher than cobalt contents but totally reverse in the spheres. Because Co and Mn precursors were present in water, the main reason seems that the permanganate may be reduced by water directly at 200°C.

$$4\ MnO_4^- + 2\ H_2O \rightarrow 4\ MnO_2 + 4\ OH^- + 3\ O_2 \qquad (2)$$

The elemental compositions of temperature-dependent materials show the drop of the Co/Mn ratios with elvated reaction temperature, indicating that reaction rates of equn (2) are faster than equn (1) at higher reaction temperature.

4-2. Conductivity enhancement with dopant and multiple mixed-valence of CMO

High conductivity of CMO was performed due to dopant and multiple oxidation states. The CMOH performed a conductivity of 4.0×10^{-4} S cm $^{-1}$, which is one order higher than those of the single oxidation state MnO_x ($10^{-5} – 10^{-6}$ S cm $^{-1}$)[61] and pure Co_3O_4. This conductivity promotion in CMOH is due to the effect of impurity doping not mixed-valence effect. In addition, CMO possess a greater conductivity of than

CMOH by two orders and pure Co_3O_4 by three orders. CMO conductivity enhancement based on the multiple mixed-valence system is more effective than single mixed-valence materials such as Co_3O_4. Multiple electron hopping make CMO to be more conductive.

4-3. Effect graphene of content in G-CMO materials

CMO with more graphene contents can enhance the conductivities and the surface areas, and these two factors play important roles in electrochemical sensing. After hybridization of graphene and CMO, producing numerous smaller pores and forming higher surface area than CMO. Due to the highly conductive feature of graphene, the conductivities of G-CMO composites were improved. The electrochemical activities of G-CMO materials are quite different and vary with the graphene content. G-CMO#1 can improve the sensitivity as well as linear range for sensing hydrogen peroxide after the 3.6 wt % of graphene hybridization. G-CMO#3 has the greatest sensitivity but lowest linear range for sensing H_2O_2 with 15.8 wt % graphene hybridization. These different activity H_2O_2 sensing may be due to the adsorbed and desorbed behaviors of the new pores produced by the graphene hybridization. CVs of H_2O_2 and ORR indicate that the current values of CMO and rGO are lower than G-CMO composites, while the onset potential values of CMO and rGO are higher

than G-CMO composites. After hybridization of graphene and CMO, the synergistic effect in G-CMO attribute to the enhanced electrochemical activities.

4-4. Nanostructure effect of CMO for hybridizing with graphene

Hybridization of CMO and graphene is highly correlated to the nanostructures in CMO. With immature nanostructure on CMO-60, the efficiency of immature G-CMO#3 for sensing H_2O_2 is lower than nanostructured G-CMO#3. In addition, the graphene content of immature G-CMO#3 is 11.3% by mass measured by TGA, which is less than G-CMO#3 by 4 %. Because the Y-shaped subunits create the void feature on CMO materials, the larger voids on CMO can be filled with more amounts of graphene. Furthermore, there are more interfaces between graphene and CMO in G-CMO#3 than immature G-CMO#3, and the resulting synergistic effect of G-CMO#3 is higher than immature G-CMO#3.

5. Conclusion

3D flower-like cobalt manganese oxide with homogeneous elemental distribution and mixed-valence feature is obtained by the redox process between cobalt (II) and manganese (VII). The sphere size and Y-shaped subunit feature can be controlled *via* reaction time and reaction temperature. High surface areas and conductivities are obtained because the Mn species are introduced in spinel cobalt oxides forming mixed-valence feature, Co (II/III) and Mn (III/IV). Two major growth pathways of equn (1) and equn (2) were highly dependent on the reaction temperatures. The redox method provides a concept with easy route to dop metal species in metal oxides for preparing high performance materials. To optimize the electrochemical activities in reduction potential region, graphene was introduced to hybridize with CMO. Surface areas and conductivities increased with the rise amounts of graphene covering on the surface of CMO. Larger voids created by Y-subunits on CMO can uptake more amounts of graphene. Due to the synergistic effect between graphene and CMO, the G-CMO showed that reductive peaks of sensing H_2O_2 and oxygen reduction reaction activity.

6. Reference

(1) Wang, Z.; Zhou, L.; David Lou, X. W. *Adv. Mater.* **2012**, *24*, 1903.

(2) Yin, Y.; Rioux, R. M.; Erdonmez, C. K.; Hughen, S.; Somorjai, G. A.; Alivisatos, A. P. *Science* **2004**, *304*, 711.

(3) Li, J.; Xiong, S.; Li, X.; Qian, Y. *Nanoscale* **2013**, *5*, 2045.

(4) Peng, X. *Adv. Mater.* **2003**, *15*, 459.

(5) Xiao, X.; Liu, X.; Zhao, H.; Chen, D.; Liu, F.; Xiang, J.; Hu, Z.; Li, Y. *Adv. Mater.* **2012**, *24*, 5762.

(6) Habas, S. E.; Lee, H.; Radmilovic, V.; Somorjai, G. A.; Yang, P. *Nat. Mater.* **2007**, *6*, 692.

(7) Li, Y.; Cai, W.; Cao, B.; Duan, G.; Sun, F.; Li, C.; Jia, L. *Nanotechnology* **2006**, *17*, 238.

(8) Li, Y.; Shen, W. *Chem. Soc. Rev.* **2014**, *43*, 1543.

(9) Li, W.-N.; Zhang, L.; Sithambaram, S.; Yuan, J.; Shen, X.-F.; Aindow, M.; Suib, S. L. *J. Phys. Chem. C* **2007**, *111*, 14694.

(10) He, T.; Chen, D.; Jiao, X.; Wang, Y. *Adv. Mater.* **2006**, *18*, 1078.

(11) He, T.; Chen, D.; Jiao, X.; Xu, Y.; Gu, Y. *Langumir* **2004**, *20*, 8404.

(12) Feng, J.; Zeng, H. C. *Chem. Mater.* **2003**, *15*, 2829.

(13) Tseng, Y.-H.; Liu, H.-Y.; Liu, M.-H.; Chen, Y.-F.; Mou, C.-Y. *J. Phys. Chem. C* **2009**, *113*, 18053.

(14) Zhou, K.; Li, Y. *Angew. Chem. Int. Ed.* **2012**, *51*, 602.

(15) Li, Y.; Hasin, P.; Wu, Y. *Adv. Mater.* **2010**, *22*, 1926.

(16) Zhang, Y.; Ma, M.; Yang, J.; Su, H.; Huang, W.; Dong, X. *Nanoscale* **2014**, *6*, 4303.

(17) Liu, X.; Qiu, G.; Li, X. *Nanotechnology* **2005**, *16*, 3035.

(18) Chen, C.-H.; Abbas, S. F.; Morey, A.; Sithambaram, S.; Xu, L.-P.; Garces, H. F.; Hines, W. A.; Suib, S. L. *Adv. Mater.* **2008**, *20*, 1205.

(19) Pang, H.; Gao, F.; Chen, Q.; Liu, R.; Lu, Q. *Dalton Trans.* **2012**, *41*, 5862.

(20) Lei, Y.; Li, J.; Wang, Y.; Gu, L.; Chang, Y.; Yuan, H.; Xiao, D. *ACS Appl. Mater. Interfaces* **2014**, *6*, 1773.

(21) Li, W.-Y.; Xu, L.-N.; Chen, J. *Adv. Funct. Mater.* **2005**, *75*, 851.

(22) Fu, C.; Li, G.; Luo, D.; Huang, X.; Zheng, J.; Li, L. *ACS Appl. Mater. Interfaces* **2014**, *6*, 2439.

(23) Lavela, P.; Tirado, J. L.; Vidal-Abarca, C. *Electrochimi. Acta* **2007**, *52*, 7986.

(24) Jiao, F.; Frei, H. *Angew. Chem. Int. Ed.* **2009**, *48*, 1841.

(25) Wee, T. L.; Sherman, B. D.; Gust, D.; Moore, A. L.; Moore, T. A.; Liu, Y.; Scaiano, J. C. *J. Am. Chem. Soc.* **2011**, *133*, 16742.

(26) Zhu, J.; Gao, Q. *Microporous Mesoporous Mater.* **2009**, *124*, 144.

(27) Wang, D.; Chen, X.; Evans, D. G.; Yang, W. *Nanoscale* **2013**, *5*, 5312.

(28) Hou, C.; Xu, Q.; Yin, L.; Hu, X. *Analyst* **2012**, *137*, 5803.

(29) Qi, X.; Gao, H.; Zhang, Y.; Wang, X.; Chen, Y.; Sun, W. *Bioelectrochemistry* **2012**, *88*, 42.

(30) Mu, J.; Zhang, L.; Zhao, M.; Wang, Y. *J. Mol. Catal. A: Chem.* **2013**, *378*, 30.

(31) Zhang, D.; Xie, Q.; Chen, A.; Wang, M.; Li, S.; Zhang, X.; Han, G.; Ying, A.; Gong, J.; Tong, Z. *Solid State Ionics* **2010**, *181*, 1462.

(32) Varkey, A. J.; Fort, A. F. *Sol. Energy Mater. Sol. Cells* **1993**, *31*, 277.

(33) Ding, Y.; Xu, L.; Chen, C.-H.; Shen, X.; Suib, S. L. *J. Phys. Chem. C* **2008**, *112*.

(34) Burriel, M.; Garcia, G.; Santiso, J.; Hansson, A. N.; Linderoth, S.; Figueras, A. *Thin Solid Films* **2005**, *473*, 98.

(35) Zhan, H. J.; Xia, Q. H.; Lu, X. H.; Zhang, Q.; Yuan, H. X.; Su, K. X.; Ma, X. T. *Catal. Commun.* **2007**, *8*, 1472.

(36) Rios, E.; Gautier, J.-L.; Poillerat, G.; Chartier, P. *Electrochimi. Acta* **1998**, *44*, 1491.

(37) Bonaccorso, F.; Lombardo, A.; Hasan, T.; Sun, Z.; Colombo, L.; Ferrari, A. C. *Mater. Today* **2012**, *15*, 564.

(38) Allen, M. J.; Tung, V. C.; Kaner, R. B. *Chem. Rev.* **2010**, *110*, 132.

(39) Geim, A. K.; Novoselov, K. S. *Nat. Mater.* **2007**, *6*, 183.

(40) Wang, Z.; Xiao, Y.; Cui, X.; Cheng, P.; Wang, B.; Gao, Y.; Li, X.; Yang, T.; Zhang, T.; Lu, G. *ACS Appl. Mater. Interfaces* **2014**, *6*, 3888.

(41) Yan, L.; Chang, Y. N.; Yin, W.; Liu, X.; Xiao, D.; Xing, G.; Zhao, L.; Gu, Z.; Zhao, Y. *Phys. Chem. Chem. Phys.* **2014**, *16*, 1576.

(42) Lu, X.; Yu, M.; Huang, H.; Ruoff, R. S. *Nanotechnology* **1999**, *10*, 296.

(43) Li, X.; Magnuson, C. W.; Venugopal, A.; Tromp, R. M.; Hannon, J. B.; Vogel, E. M.; Colombo, L.; Ruoff, R. S. *J. Am. Chem. Soc.* **2011**, *133*, 2816.

(44) Kim, K. S.; Zhao, Y.; Jang, H.; Lee, S. Y.; Kim, J. M.; Ahn, J. H.; Kim, P.; Choi, J. Y.; Hong, B. H. *Nature* **2009**, *457*, 706.

(45) Hasan, T.; Torrisi, F.; Sun, Z.; Popa, D.; Nicolosi, V.; Privitera, G.; Bonaccorso, F.; Ferrari, A. C. *Phys. Status Solidi. B* **2010**, *247*, 2953.

(46) Torrsi, F.; Hasan, T.; Wu, W.; Sun, Z.; Lombardo, A.; Kulmala, T. S.; Hsieh, G.-W.; Jung, S.; Bonaccorso, F.; Paul, P. J.; Chu, D.; Ferrari, A. C. *ACS Nano* **2012**, *6*, 2992.

(47) Srivastava, K. P.; Ghosh, S. *Appl. Phys. Lett.* **2013**, *102*, 043102.

(48) Hummers, W. S.; Offeman, R. E. *J. Am. Chem. Soc.* **1958**, 1339.

(49) Dikin, D. A.; Stankovich, S.; Zimney, E. J.; Piner, R. D.; Dommett, G. H.; Evmenenko, G.; Nguyen, S. T.; Ruoff, R. S. *Nature* **2007**, *448*, 457.

(50) Feng, H.; Cheng, R.; Zhao, X.; Duan, X.; Li, J. *Nat. Commun.* **2013**, *4*, 1539.

(51) Fan, Z.-J.; Kai, W.; Yan, J.; Wei, T.; Zhi, L.-J.; Feng, J.; Ren, Y.-M.; Song, L.-P.; Wei, F. *ACS Nano* **2011**, *5*, 191.

(52) Zhang, Z.; Hao, J.; Yang, W.; Lu, B.; Ke, X.; Zhang, B.; Tang, J. *ACS Appl. Mater. Interfaces* **2013**, *5*, 3809.

(53) Su, Y.; Zhu, Y.; Yang, X.; Shen, J.; Lu, J.; Zhang, X.; Chen, J.; Li, C. *Ind. Eng. Chem. Res.* **2013**, *52*, 6076.

(54) Li, D.; Shi, D.; Chen, Z.; Liu, H.; Jia, D.; Guo, Z. *RSC Adv.* **2013**, *3*, 5003.

(55) Liang, Y.; Li, Y.; Wang, H.; Zhou, J.; Regier, T.; Dai, H. *Nat. Mater.* **2011**, *10*, 780.

(56) Lan, W. J.; Kuo, C. C.; Chen, C. H. *Chem. Commun.* **2013**, *49*, 3025.

(57) Njagi, E. C.; Chen, C.-H.; Genuino, H.; Galindo, H.; Huang, H.; Suib, S. L. *Appl. Catal., B* **2010**, *99*, 103.

(58) Tian, Z.-Y.; Tchoua Ngamou, P. H.; Vannier, V.; Kohse-Höinghaus, K.; Bahlawane, N. *Appl. Catal., B* **2012**, *117-118*, 125.

(59) Lv, X.-J.; Fu, W.-F.; Chang, H.-X.; Zhang, H.; Cheng, J.-S.; Zhang, G.-J.; Song, Y.; Hu, C.-Y.; Li, J.-H. *J. Mater. Chem.* **2012**, *22*, 1539.

(60) Akhavan, O. *ACS Nano* **2011**, *4*, 4174.

(61) Kayan, A.; Tarcan, E.; Kadiroglu, U.; Esmer, K. *Mater. Lett.* **2004**, *58*, 2170.